

# Weyl magnons in noncoplanar stacked kagomé antiferromagnets

S. A. Owerre<sup>1</sup>

<sup>1</sup>*Perimeter Institute for Theoretical Physics, 31 Caroline St. N., Waterloo, Ontario N2L 2Y5, Canada.*

(Dated: December 11, 2022)

Weyl nodes have been realized experimentally in photonic, electronic, and phononic crystals. However, magnonic Weyl nodes have not been experimentally verified. Unfortunately, the existing theoretical predictions of Weyl magnon nodes in pyrochlore (anti)ferromagnets involve nodes at high energy above the lowest excitation possibly prohibiting an experimental observation due to the population effect of bosonic quasiparticles in the lowest excitation at low temperatures. In this paper, we propose an experimentally accessible Weyl magnon nodes in the stacked frustrated noncoplanar kagome antiferromagnets as realized in various real materials. In stark contrast to the existing predictions, the present Weyl nodes do not rely on time-reversal symmetry breaking by the magnetic order, rather they result from explicit macroscopically broken time reversal symmetry by the scalar spin chirality of noncoplanar spin textures, and can be generalized to chiral spin liquid states. The scalar spin chirality gives a real space Berry curvature which is not available in other systems. We show the existence of magnon arc surface states connecting projected Weyl magnon nodes on the surface Brillouin zone. Most importantly, the Weyl nodes occur at the lowest excitation and carry the dominant contribution to the topological (anomalous) thermal Hall effect. We also uncover the first realization of triply degenerate nodal-line magnons when the scalar spin chirality is zero and the out-of-plane Dzyaloshinskii-Moriya interaction is nonzero.

Geometrically frustrated kagomé antiferromagnets are the most studied quantum magnetic systems in condensed matter physics, due to their unconventional properties such as the possibility of quantum spin liquids [1–3], where magnetic long-range order is forbidden by frustrated interactions down to the lowest temperatures. However, emerging experimental studies have shown that various frustrated kagomé antiferromagnets show evidence of intrinsic or magnetic-field-induced magnetic long-range order at low temperatures [4–8]. The presence of magnetic long-range order in frustrated kagomé antiferromagnets can be as a result of intrinsic perturbative anisotropy such as the Dzyaloshinskii-Moriya interaction (DMI) [9, 10]. The DMI is a consequence of spin-orbit coupling (SOC) and it is present in magnetic systems that lack an inversion center. Interestingly, it is intrinsic to kagomé materials [4–8, 11–13]. In the magnetically ordered phase, magnons are the quasiparticle excitations. They are neutrally charged and obey Bose

statistics. They can also transport heat, spin current, and carry a spin of 1. These properties make magnons potential candidates for spintronics and magnetic data storage applications [14].

Recently, the concepts of electronic Weyl semimetals (WSMs) [15, 16] have emerged as the new theme in condensed matter physics which have been realized experimentally [17, 18], with numerous potential technological applications. They are the first realization of Weyl fermions in condensed matter systems. In principle, Weyl nodes are allowed in three-dimensional (3D) solid-state crystals with either broken inversion symmetry or time-reversal symmetry (TRS). Nonetheless, materials hosting intrinsic Weyl nodes are elusive in nature. In fact, the first experimental evidence of Weyl nodes was realized in an artificial photonic crystal [19], and recently in phononic crystal [20], both of which have the same Bose statistics as magnons. Recently, this concept has been theoretically extended to magnon bands in the breathing pyrochlore antiferromagnets [21] and collinear ferromagnets [22–25], but an explicit experimental verification has not been reported, possibly because the promising ones in pyrochlore (anti)ferromagnets involve nodes at high energy above the lowest excitation, which should be thermally populated at low temperatures.

In principle, ferromagnetic and antiferromagnetic Weyl magnons (WMs) are different as the latter can occur in the absence of DMI. Moreover, antiferromagnets have zero spin magnetization which makes their magnetism externally invisible and insensitive to external magnetic fields, therefore are more efficient in spintronics applications [26]. Thus far, the breathing antiferromagnets is the only antiferromagnetic system exhibiting WM nodes [21], but their existence in this system is not very clear as they rely on the broken TRS by the magnetic order. As every magnetically ordered system breaks TRS, we definitely do not expect all of them to exhibit Weyl nodes. Therefore the mechanism for WMs to exist in antiferromagnetic systems is still an open question and requires further investigation as corroborated by the authors [21]. Moreover, recent study shows that the DMI can induce gapped topological magnon bands in pyrochlore antiferromagnets [27]. Hence, it is valid to say that the WMs in pyrochlore antiferromagnets may not be robust against the DMI [28], which contradicts the concept of Weyl nodes as robust topological objects.

In this paper, we predict the existence of different, robust WMs in stacked frustrated kagomé antiferromagnets naturally available in real materials. This system is endowed with a  $120^\circ$  noncollinear spin structure due to intrinsic out-of-plane DMI or easy-plane anisotropy

or intralayer antiferromagnetic next-nearest-neighbour (NNN) interaction, as realized in real frustrated kagomé materials [4–8]. As the conventional  $120^\circ$  noncollinear spin structure has zero scalar spin chirality and preserves certain symmetries of the kagomé lattice, we find no WMs despite broken TRS by the magnetic order. This is in contrast to previous speculation in antiferromagnets [21]. However, the magnon bands in this case form doubly degenerate nodal-line magnons (DDNLMs) and triply degenerate nodal-line magnons (TDNLMs). We argue that the nodal-line magnons are due to an “effective TRS” (i.e. time-reversal symmetry plus spin rotational and/or mirror reflection symmetry), which is preserved by the conventional  $120^\circ$  noncollinear spin structure. The new TDNLMs or three-component bosons have not been previously proposed in insulating magnets, but they have been realized in fermionic systems [29–32] as condensed matter quasiparticles are not constrained by Lorentz invariance. In stark contrast to DDNLMs in ferromagnets with zero DMI [24, 33], the new TDNLMs in the conventional  $120^\circ$  noncollinear spin structure require the out-of-plane DMI for stability.

The existence of Weyl nodes do not necessarily require any special symmetry protection. Weyl nodes appear in pairs of opposite chirality, and can be separated in momentum space when TRS is broken [16]. In the current study, a slightly canted  $120^\circ$  spin structure along the out-of-plane stacking direction form noncoplanar chiral spin texture with a nonzero scalar spin chirality, which breaks TRS explicitly and macroscopically. In real materials, noncoplanar chiral spin texture can be induced either by an external magnetic field applied normal to the conventional  $120^\circ$  noncollinear spin structure or by a small in-plane DMI due to lack of mirror symmetry. In both cases the noncoplanar spin canting has the same effect. Therefore, we consider the former case in this main text and the latter case in the Supplementary information. This leads to the decay of nodal-line magnons into pairs of WM nodes, which form Weyl cones on the (010) surface Brillouin zone. They come in pairs of opposite chirality and possess chiral magnon surface states (magnon arc) connecting two projected WM nodes on the (010) surface.

Furthermore, in contrast to pyrochlore systems [21–23], the current WM nodes come from the lowest excitation, which makes them experimentally feasible due to the population effect of bosonic quasiparticles at low temperatures, and they carry the dominant contribution to the topological (anomalous) thermal Hall effect (see Supplementary information). They are, indeed, robust as all the dominant perturbations have been taken into account. The current results show that robust WMs require macroscopically broken TRS as opposed to broken TRS by magnetic order in pyrochlore antiferromagnets. We also find that the WM nodes are always present in the noncoplanar regime provided the interlayer coupling is nonzero. This establishes that both 3D and quasi-2D frustrated kagomé antiferromagnets are candidates for in-

vestigating antiferromagnetic WMs. As the interlayer coupling always exist in realistic kagomé antiferromagnetic materials, the current prediction of WMs can be experimentally accessible by inelastic neutron scattering experiments.

## Results

**Model.** We study stacked frustrated kagomé antiferromagnets governed by the Hamiltonian

$$\mathcal{H} = J \sum_{\langle ij \rangle, \ell} \mathbf{S}_{i, \ell} \cdot \mathbf{S}_{j, \ell} + \sum_{\langle ij \rangle, \ell} \mathbf{D}_{ij} \cdot \mathbf{S}_{i, \ell} \times \mathbf{S}_{j, \ell} + J_c \sum_{i, \langle \ell \ell' \rangle} \mathbf{S}_{i, \ell} \cdot \mathbf{S}_{i, \ell'} - H \sum_{i, \ell} S_{i, \ell}^z, \quad (1)$$

where  $i$  and  $j$  denote the sites on the layers,  $\ell$  and  $\ell'$  label the layers. The first term is the intralayer antiferromagnetic nearest-neighbour (NN) Heisenberg interaction. The second term is a perturbative anisotropy to the Heisenberg interaction, which is dominated by the out-of-plane DMI ( $\mathbf{D}_{ij} = \pm D_z \hat{\mathbf{z}}$ ) due to lack of inversion symmetry between two sites on each layer. The DMI alternates between the triangular plaquettes of the kagomé lattice as shown in Fig. 1(a). The out-of-plane DMI stabilizes the  $120^\circ$  noncollinear spin structure and its sign determines the vector chirality of the noncollinear spin order [11, 12]. The third term is the interlayer NN interaction between the layers which can be ferromagnetic ( $J_c < 0$ ) or antiferromagnetic ( $J_c > 0$ ). Finally, the last term is an external magnetic field in units of  $g\mu_B$ , along the stacking direction taken as the  $z$ -axis. Without loss of generality, we consider unshifted stacked kagomé layers as realized in different stacked frustrated kagomé antiferromagnets [5–8]. Note that the global  $\text{SO}(3)$  spin rotational symmetry of Eq. 1 is broken down to  $\text{SO}(2)$  or  $\text{U}(1)$  spin rotational symmetry in the  $x$ - $y$  plane or about the  $z$ -axis respectively. In the following we consider antiferromagnetic interlayer coupling ( $J_c > 0$ ). The analysis for ferromagnetic interlayer coupling ( $J_c < 0$ ) is given in Methods.

**Nodal-line magnons.** Now, we study the magnon bands of stacked frustrated kagomé antiferromagnets. In order to do this, we rotate our spin quantization axis locally in spin space so that it aligns with the magnetic ordering; then we introduce the Holstein-Primakoff bosons (see Methods). In the limit of zero magnetic field ( $H = 0$ ) and zero DMI ( $D_z = 0$ ), the magnon bands of stacked frustrated kagomé antiferromagnets show zero modes for specific values of out-of-plane momentum  $k_z$  [34, 35]. Therefore the absence of magnetic long-range order in the 2D frustrated kagomé antiferromagnets also persists in the 3D limit. As shown in Fig. 2, a nonzero DMI lifts the zero energy mode for all  $k_z$ , thereby stabilizes the 3D  $120^\circ$  noncollinear spin configuration as in the 2D system [11]. However, the magnon bands in the 3D or quasi-2D (with nonzero  $J_c$ ) system form nodal-line magnons along  $\mathbf{K}$ - $\mathbf{H}$  and  $\mathbf{A}$ - $\mathbf{\Gamma}$  lines of the Brillouin zone (Fig. 1(b) and (c)) as depicted in Fig. 2a. In the weakly coupled realistic regime  $J_c/J < 1$ , there are DDNLMs

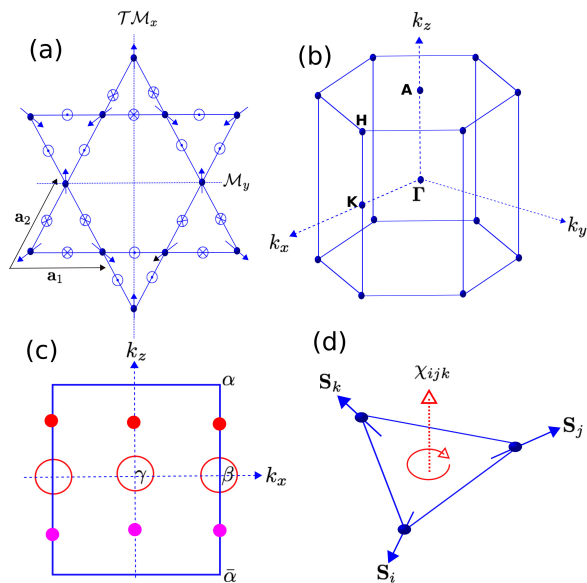


FIG. 1: **Kagomé lattice, bulk and surface Brillouin zone, and scalar spin chirality.** (a) Top view of unshifted kagomé lattice stacked along the (001) direction. The  $120^\circ$  noncollinear spin configuration with a positive vector chirality is indicated (blue arrows). The in-plane unit vectors are  $\mathbf{a}_1 = (1, 0, 0)$  and  $\mathbf{a}_2 = (1/2, \sqrt{3}/2, 0)$ . The unit vector along the stacking direction  $\mathbf{a}_3 = (0, 0, 1)$  is not depicted. The mirror reflection axes (dotted lines) and the direction of DMI (crossed and dotted circles) are indicated. (b) Bulk Brillouin zone (BZ) of stacked hexagonal lattice with indicated high-symmetry points. (c) (010) surface BZ with TDNLMs (open red circles) and WM nodes (filled red and pink circles). The  $(k_x, k_z)$  coordinates are  $\gamma = (0, 0)$ ,  $\beta = (2\pi/3, 0)$ ,  $\alpha = (2\pi/3, \pi)$ ,  $\bar{\alpha} = (2\pi/3, -\pi)$ . (d) Scalar spin chirality of three noncoplanar spins on a triangle:  $\chi_{ijk} = \mathbf{S}_i \cdot (\mathbf{S}_j \times \mathbf{S}_k)$  (dash red arrow).

along  $\mathbf{K}$ – $\mathbf{H}$  and TDNLMs along  $\mathbf{A}$ – $\mathbf{\Gamma}$ . However, in the strongly coupled regime  $J_c/J > 1$  (probably unrealistic), there are only TDNLMs along  $\mathbf{K}$ – $\mathbf{H}$  and  $\mathbf{A}$ – $\mathbf{\Gamma}$  lines (not shown). The TDNLMs (or three-component bosons) are the analogs of fermionic counterparts [29–32]. They are allowed as condensed matter quasiparticles are not constrained by Lorentz invariance.

The nodal-line magnons in the conventional  $120^\circ$  noncollinear spin structure can be understood as follows. For a perfect kagomé lattice with strong out-of-plane DMI the ground state of the Hamiltonian Eq. 1 at zero field is a  $120^\circ$  noncollinear spin structure with positive vector chirality and zero scalar spin chirality as depicted in Fig. 1a. This noncollinear spin structure preserves all the symmetries of the kagomé lattice. For instance, the combination of TRS ( $\mathcal{T}$ ) and  $180^\circ$  spin rotation of the in-plane coplanar spins about the  $z$ -axis,  $\mathcal{R}_z(\theta)$ , is a good symmetry. In addition, mirror reflection symmetry of the kagomé plane about the  $x$  or  $y$  axis in combination with  $\mathcal{T}$  (i.e.  $\mathcal{T}\mathcal{M}_x\mathcal{T}$  or  $\mathcal{M}_y\mathcal{T}$ ) is also a symmetry of the  $120^\circ$  noncollinear spin structure. These symme-

tries are referred to as an “effective TRS” and lead to nodal-line magnons. They are different from the nodal-line magnons in insulating ferromagnets [24, 33] by the presence of the DMI and triply degeneracy.

**Weyl magnons.** We now study the possibility of WMs in the stacked frustrated kagomé antiferromagnets. As in electronic systems, Weyl nodes do not necessarily require any special symmetry protection. They are formed by non-degenerate bands and appear in pairs of opposite chirality, and can be separated in momentum space when TRS is broken. Now, we will break the “effective TRS” and study its effects on the magnon bands. There are two ways in which this symmetry can be broken. The first one is intrinsic when the kagomé lattice lacks a mirror reflection symmetry. Therefore, a small in-plane DMI will be allowed and induces noncoplanar chiral spin textures [4] (see also Supplementary information). However, in most frustrated kagomé antiferromagnets, e.g. herbertsmithite [13], the in-plane DMI can be quite negligible. The second one is extrinsic by applying an out-of-plane external magnetic field perpendicular to the in-plane  $120^\circ$  spin structure. This also induces noncoplanar chiral spin textures with a nonzero scalar spin chirality given by  $\chi_{ijk;l} = \mathbf{S}_{i,\ell} \cdot (\mathbf{S}_{j,\ell} \times \mathbf{S}_{k,\ell})$  as shown in Fig. 1(d) (see Methods). The canting angle and the scalar spin chirality play the same role in both cases.

However, the magnetic-field-induced  $\chi_{ijk;l}$  persists even when the in-plane magnetic order is stabilized by other perturbative interactions different from the DMI, e.g. easy-plane anisotropy [36] or intralayer antiferromagnetic NNN [37]. Therefore, we expect that WMs should also exist in stacked noncoplanar chiral antiferromagnets without the DMI. This noncoplanar chiral spin texture breaks TRS macroscopically, hence we can now look for the existence of WMs. We have confirmed the existence of WM nodes in the noncoplanar regime in Fig. 2b. We see that the nodal-line magnons give way for WM nodes. The lowest and middle non-degenerate magnon bands cross linearly in the weakly coupled realistic limit  $J_c < J$ , and form three pairs of WM cones on the (010) surface located at  $(\pm 2\pi/3, 0, \pm k_W^1)$  and  $(0, 0, \pm k_W^2)$ . In the strongly coupled regime  $J_c \geq J$  (probably unrealistic), we also find that the lowest and middle magnon bands cross linearly at  $(\pm 2\pi/3, 0, \pm k_W^1)$  and  $(0, 0, \pm k_W^2)$ . Additionally, the topmost and lowest magnon bands cross linearly at  $(\pm 2\pi/3, 0, \pm k_W^3)$  and  $(0, 0, \pm k_W^4)$  (see Methods). In this case the  $W_3$  WM nodes form analogs of type-II WSM [38] (see Methods). The positions of the WM nodes  $k_W^i$  are determined explicitly (see Methods). Most importantly, we find that WM nodes always exist in the noncoplanar regime for all nonzero values of  $J_c/J$  (see Methods). This suggests that both 3D and quasi-2D stacked kagomé antiferromagnets are candidates for WM nodes.

It is crucial to point out that the WM nodes in stacked frustrated kagomé antiferromagnets are different from those of breathing pyrochlore antiferromagnets [21]. The latter requires no DMI and rely on broken TRS by the

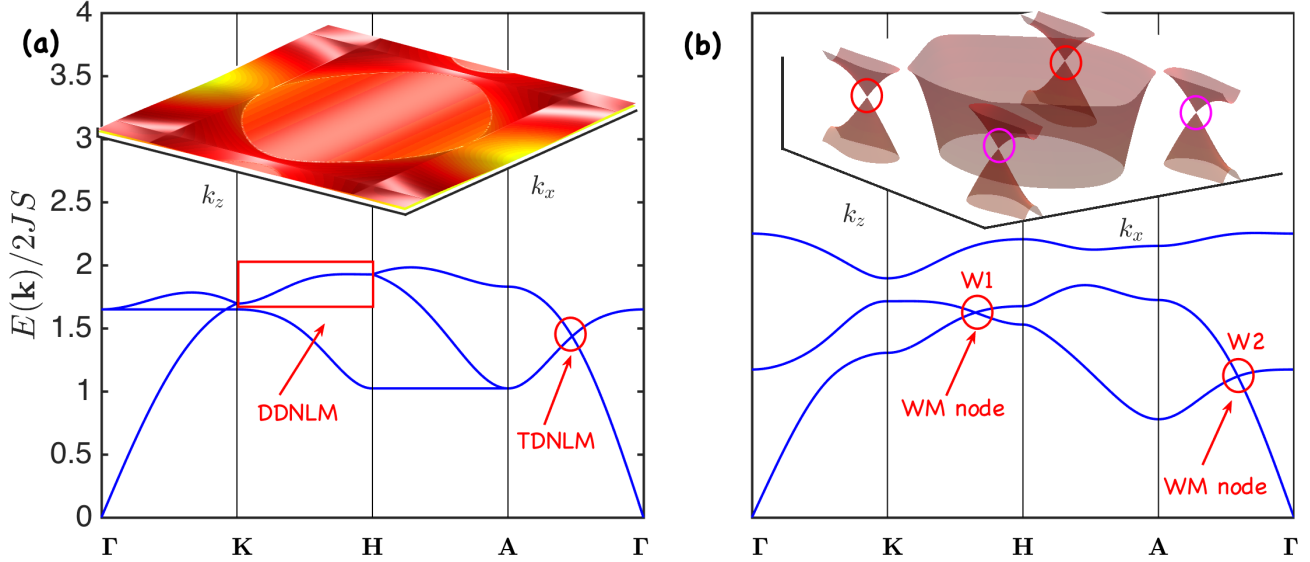


FIG. 2: **Magnon bands of antiferromagnetically coupled stacked kagomé antiferromagnets.** (a) Doubly (red rectangle) and triple (red circle) degenerate nodal-line magnon bands without scalar spin chirality for  $D_z/J = 0.2$ ,  $J_c/J = 0.5$ ,  $H = 0$ . Inset shows 3D magnon bands in the  $k_y = 0$  plane with nodal magnon rings in the  $k_x$ - $k_z$  momentum space. (b) Weyl magnon bands of stacked frustrated kagomé antiferromagnets with scalar spin chirality for  $D_z/J = 0.2$ ,  $J_c/J = 0.5$ ,  $H = 0.3H_s$ ,  $H_s = 6J + 2\sqrt{3}D_z + 4J_c$  is the saturation field. Inset shows 3D magnon bands in the  $k_y = 0$  plane for  $W_1$  Weyl cones.

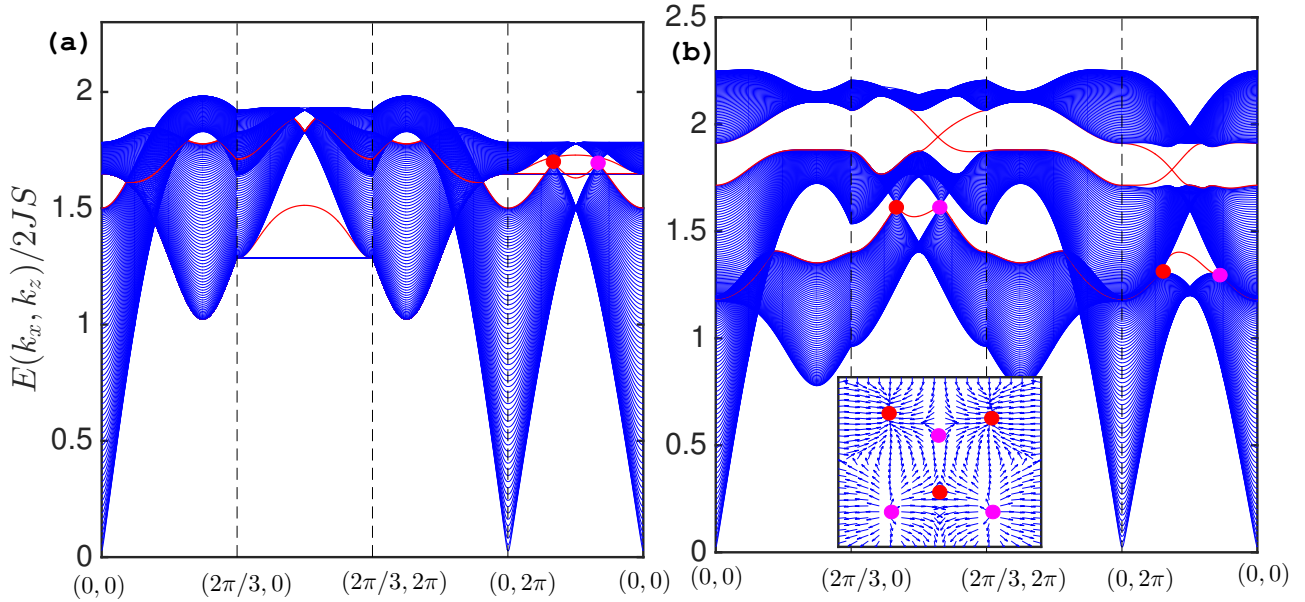


FIG. 3: **Nodal-line and Weyl magnons with drumhead and magnon arc surface states respectively.** (a) (010)-projected nodal-line magnons (red and pink dots) with drumhead magnon surface states (red lines) at zero scalar spin chirality with the parameters of Fig .2a. (b). (010)-projected Weyl magnon nodes of opposite chirality (red and pink dots) connected by chiral magnon arc surface states (red lines) at nonzero scalar spin chirality with the parameters of Fig .2b. Inset shows the monopole (red dot) and antimonopole (pink dot) distribution of the lowest magnon band Berry curvature projected on the (010) surface.

magnetic order. However, as every magnetically ordered system breaks TRS, we do not expect every ordered magnetic system to have WM nodes. Moreover, gapped topological magnon bands were recently found in pyrochlore antiferromagnets with DMI [27]. This suggests that the WMs in breathing pyrochlore antiferromagnets may not be robust when all the proper DMIs are taken into account [28]. In the current study, however, the only requirement for the existence of WM nodes is the macroscopically broken TRS by  $\chi_{ijk;l}$ , which can be induced by the in-plane DMI (see Supplementary information) or an external magnetic field as shown here in addition to the out-of-plane DMI. They also persist even in the absence of DMI as 120° noncollinear magnetic order can be stabilized through other means. As we mentioned above, our results show that WMs should not be allowed in every magnetically ordered system that breaks TRS by the magnetic order. Indeed, the current WM nodes are robust as all the dominant perturbations have been taken into account.

**Magnon surface states.** The topological protection of WMs is also encoded in the magnon arc surface states. Let us consider the (010) surface and assume that the system is infinite along  $x$  and  $z$  directions, so both  $k_x$  and  $k_z$  are good quantum numbers. As shown in Fig. 3a the (010)-projected nodal-line magnons at zero scalar spin chirality have drumhead magnon surface states (red lines). In the noncoplanar regime the nodal-line magnons give way for WM nodes. As shown in Fig. 3b, (010)-projected WM nodes of opposite chirality (red and pink dots) are connected by magnon arc surface states. Also note that in this weakly coupled realistic regime ( $J_c < J$ ) the middle and topmost bands also feature a topological (Chern) magnon insulator (TMI) with gapless surface states between the bulk gaps. The inset of Fig. 3b shows that the WM nodes act as monopole (source) and anti-monopole (sink) of the Berry curvature with chirality 1 (red dot) and  $-1$  (pink dot) respectively. Note that in contrast to other systems, the Berry curvature in the current system is already present in the real space spin configuration due to  $\chi_{ijk;l}$  as depicted in Fig. 1 (d). For  $-k_W^i < |k_z| < k_W^i$  the system is gapped and can be considered as slices of 2D TMIs [39]. In this case there are definite Chern numbers in the  $k_x$ - $k_y$  plane for fixed  $k_z$ , estimated as  $C_{1,2}(-k_W^i < |k_z| < k_W^i) = \pm \text{sgn}(\sin(\phi))$  for the first two bands and  $C_3(-k_W^i < |k_z| < k_W^i) = 0$  for the topmost band, where  $\phi$  is the angle subtended by

three noncoplanar spins in a unit triangle (see Methods), and  $\sin \phi$  is proportional to  $\chi_{ijk}$  (see Fig. 1d).

### Conclusion

We have shown that stacked frustrated kagomé antiferromagnets are complete topological magnon “semimetals” hosting doubly and triply degenerate nodal-line magnons at nonzero DMI and zero scalar spin chirality, which transform into Weyl magnon nodes at nonzero scalar spin chirality with finite topological (anomalous) thermal Hall effect. The currently predicted Weyl magnon nodes do not rely on broken TRS by the magnetic order, instead they are provided by explicit macroscopically broken TRS by the scalar spin chirality. Therefore, the concept of Weyl nodes may exist in chiral spin liquids states [40, 41], where TRS is spontaneously broken by the scalar spin chirality. As we noted above, noncoplanar chiral spin textures are intrinsic to realistic frustrated kagomé materials with both in-plane and out-of-plane DMI. Hence, the present Weyl magnon nodes are, indeed, robust as all the dominant perturbations have been taken into account. As the Weyl magnon nodes occur at the lowest excitation they are the dominant contribution to the topological (anomalous) thermal Hall effect as shown in the Supplementary information. We believe that our prediction of Weyl magnon nodes in stacked (3D and quasi-2D) noncoplanar chiral spin textures is the most promising candidates towards an experimental realization of Weyl magnon nodes in (un)frustrated magnets. They can be investigated using the inelastic neutron scattering. Here, we considered noncollinear spin structure with positive vector chirality, however our results should also exist in magnetic systems with negative vector chirality as recently reported in an insulating stacked kagomé antiferromagnets [42], and also in metallic frustrated magnets  $\text{Mn}_3\text{Sn}/\text{Ge}$  [43–45] with metallic Weyl nodes [46, 47], but in this case the spins cant in-plane with zero scalar spin chirality.

**Note added.** Upon arXiv submission of this manuscript, we became aware of a recent study Ref. [48], where the authors adopted the easy-plane breathing pyrochlore antiferromagnetic model in Ref. [21], and studied WMs in the easy-axis counterpart with all-in-all-out (AIAO) magnetic ordering with zero scalar spin chirality. Therefore, this system also rely on broken TRS by the magnetic order and they are obviously different from the current results in noncoplanar stacked kagomé antiferromagnets with nonzero scalar spin chirality.

- 
- [1] Norman, M. R. Herbertsmithite and the search for the quantum spin liquid. *Rev. Mod. Phys.* **88**, 041002 (2016).
  - [2] Zhou, Y., Kanoda, K. & Ng, T. -K. Quantum spin liquid states. *Rev. Mod. Phys.* **89**, 025003 (2017).
  - [3] Savary L. & Balents, L. Quantum spin liquids: a review. *Rep. Prog. Phys.* **80**, 016502 (2017).
  - [4] Grohol D. et al. Spin chirality on a two-dimensional frustrated lattice. *Nat. Mater.* **4**, 323 (2005).
  - [5] Zheng X. G. et al. Antiferromagnetic transitions in polymorphous minerals of the natural cuprates atacamite and botallackite  $\text{Cu}_2\text{Cl}(\text{OH})_3$ . *Phys. Rev. B* **71**, 174404 (2005).
  - [6] Zheng X. G. et al. Coexistence of Long-Range Order and Spin Fluctuation in Geometrically Frustrated Clinoatacamite  $\text{Cu}_2\text{Cl}(\text{OH})_3$ . *Phys. Rev. Lett.* **95**, 057201 (2005).
  - [7] Han, T.-H., Singleton, J. & Schlueter, J. A. Barlowite: A

- Spin-1/2 Antiferromagnet with a Geometrically Perfect Kagome Motif. *Phys. Rev. Lett.* **113**, 227203 (2014).
- [8] Han T.-H. et al. Anisotropy: Spin order and magnetization of single-crystalline  $\text{Cu}_4(\text{OH})_6\text{FBr}$  barlowite. *Phys. Rev. B* **93**, 214416 (2016).
- [9] Dzyaloshinsky, I. A thermodynamic theory of “weak” ferromagnetism of antiferromagnetics. *J. Phys. Chem. Solids* **4**, 241 (1958).
- [10] Moriya, T. Anisotropic Superexchange Interaction and Weak Ferromagnetism. *Phys. Rev.* **120**, 91 (1960).
- [11] Elhajal, M., Canals, B. & Lacroix, C. Symmetry breaking due to Dzyaloshinsky-Moriya interactions in the kagomé lattice. *Phys. Rev. B* **66**, 014422 (2002).
- [12] C epas O. et al. Quantum phase transition induced by Dzyaloshinskii-Moriya interactions in the kagome antiferromagnet. *Phys. Rev. B* **78**, 140405(R) (2008).
- [13] Zorko A. et al. Dzyaloshinsky-Moriya Anisotropy in the Spin-1/2 Kagome Compound  $\text{ZnCu}_3(\text{OH})_6\text{Cl}_2$ . *Phys. Rev. Lett.* **101**, 026405 (2008).
- [14] Chumak A. V. et al. Magnon spintronics. *Nat. Phys.* **11**, 453 (2015).
- [15] Wan, X. et al. Topological semimetal and Fermi-arc surface states in the electronic structure of pyrochlore iridates. *Phys. Rev. B* **83**, 205101 (2011)
- [16] Burkov A. A. and Balents L. Weyl Semimetal in a Topological Insulator Multilayer. *Phys. Rev. Lett.* **107**, 127205 (2011).
- [17] Xu S.-Y. et al. Discovery of a Weyl fermion semimetal and topological Fermi arcs. *Science* **349**, 613 (2015).
- [18] Lv B.-Q. et al. Experimental Discovery of Weyl Semimetal TaAs. *Phys. Rev. X* **5**, 031013 (2015).
- [19] Lu L. et al. Experimental observation of Weyl points. *Science* **349**, 622 (2015).
- [20] Li F. et al. Weyl points and Fermi arcs in a chiral phononic crystal. *Nat. Phys.* (2017) doi:10.1038/nphys4275
- [21] Li F.-Y. et al. Weyl magnons in breathing pyrochlore antiferromagnets. *Nat. Commun.* **7**, 12691 (2016).
- [22] Mook, A., Henk, J. & Mertig, I. Tunable magnon Weyl points in ferromagnetic pyrochlores. *Phys. Rev. Lett.* **117**, 157204 (2016).
- [23] Ying, S., Wang, X. S. & Wang, X. R. Magnonic Weyl semimetal and chiral anomaly in pyrochlore ferromagnets. *Phys. Rev. B* **95**, 224403 (2017).
- [24] Li K. & Hu, J. Weyl and Nodal Ring Magnons in Three-Dimensional Honeycomb Lattices. *Chin. Phys. Lett.* **34**, 077501 (2017).
- [25] Su, Y. & Wang, X. R. Chiral anomaly of Weyl magnons in stacked honeycomb ferromagnets. arXiv:1705.04164 (2017).
- [26] Smejkal, L., Jungwirth, T. & Sinova. Route towards Dirac and Weyl antiferromagnetic spintronics. *J. Phys. Status Solidi RRL* **11**, 1700044 (2017).
- [27] Laurell, P. & Fiete, G. A. Topological Magnon Bands and Unconventional Superconductivity in Pyrochlore Iridate Thin Films. *Phys. Rev. Lett.* **118**, 177201 (2017).
- [28] The robustness of Weyl magnons against the DMIs in pyrochlore antiferromagnets is currently not investigated.
- [29] Bradlyn B. et al. Beyond Dirac and Weyl fermions: Unconventional quasiparticles in conventional crystals. *Science* **353**, aaf5037 (2016).
- [30] Weng H. et al. Topological semimetals with triply degenerate nodal points in  $\theta$ -phase tantalum nitride. *Phys. Rev. B* **93**, 241202 (2016).
- [31] Zhu Z. et al. Triple Point Topological Metals. *Phys. Rev. X* **6**, 031003 (2016).
- [32] Lv B. Q. et al. Observation of three-component fermions in the topological semimetal molybdenum phosphide. *Nature* **546**, 627 (2017).
- [33] Mook A., Henk, J. & Mertig, I. Magnon nodal-line semimetals and drumhead surface states in anisotropic pyrochlore ferromagnets. *Phys. Rev. B* **95**, 014418 (2017).
- [34] Schmalfuss, D., Richter, J. & Ihle, D. Absence of long-range order in a spin-half Heisenberg antiferromagnet on the stacked kagom e lattice. *Phys. Rev. B* **70**, 184412 (2004).
- [35] G tze O. & Richter, J. The route to magnetic order in the spin-1/2 kagome Heisenberg antiferromagnet: The role of interlayer coupling. *EPL (Europhys. Lett.)* **114**, 67004 (2016).
- [36] Chernyshev A. L. , & Zhitomirsky M. E. Quantum Selection of Order in an XXZ Antiferromagnet on a Kagome Lattice. *Phys. Rev. Lett.* **113**, 237202 (2014).
- [37] Harris A. B., Kallin C., & Berlinsky A. J. Possible N eel orderings of the Kagom e antiferromagnet. *Phys. Rev. B* **45**, 2899 (1992).
- [38] Soluyanov A. A. et al. Type-II Weyl semimetals. *Nature* **527**, 495 (2015)
- [39] Owerre S. A. topological (anomalous) thermal Hall effect in frustrated kagome antiferromagnets. *Phys. Rev. B* **95**, 014422 (2017).
- [40] Hermanns, M., O’Brien, K. & Trebst, S. Weyl Spin Liquids. *Phys. Rev. Lett.* **114**, 157202 (2015).
- [41] Hermanns, M., O’Brien, K. & Trebst, S. Classification of gapless  $\mathbb{Z}_2$  spin liquids in three-dimensional Kitaev models. *Phys. Rev. B* **93**, 085101 (2016).
- [42] Okuma R. et al. Weak ferromagnetic order breaking the threefold rotational symmetry of the underlying kagom e lattice in  $\text{CdCu}_3(\text{OH})_6(\text{NO}_3)_2\text{H}_2\text{O}$ . *Phys. Rev. B* **95**, 094427 (2017).
- [43] Chen, H., Niu Q., & MacDonald A. H. Anomalous Hall effect arising from noncollinear antiferromagnetism. *Phys. Rev. Lett.* **112**, 017205 (2014).
- [44] Nakatsuji S., Kiyohara N. & Higo T. Large anomalous Hall effect in a non-collinear antiferromagnet at room temperature. *Nature* **527**, 212 (2015).
- [45] Nayak A. K. et al. Large anomalous Hall effect driven by a nonvanishing Berry curvature in the noncolinear antiferromagnet  $\text{Mn}_3\text{Ge}$ . *Sci. Adv.* **2** e1501870 (2016).
- [46] Yang H. et al. Topological Weyl semimetals in the chiral antiferromagnetic materials  $\text{Mn}_3\text{Ge}$  and  $\text{Mn}_3\text{Sn}$ . *New J. Phys.* **19** 015008 (2017).
- [47] K ubler J. & Felser, C. Non-collinear antiferromagnets and the anomalous Hall effect. *EPL (Europhys. Lett.)* **108**, 67001 (2014).
- [48] Jian S.-K. & Nie, W. Weyl magnons in pyrochlore antiferromagnets with all-in-all-out orders. arXiv:1708.02948 (2017).

**Acknowledgments.** Research at Perimeter Institute is supported by the Government of Canada through Industry Canada and by the Province of Ontario through the Ministry of Research and Innovation.

#### Author contributions

S. A. Owerre conceived the idea, performed the calcu-

lations, discussed the results, and wrote the manuscript.

### Additional information

Supplementary information accompany this manuscript.

### Competing financial interests

The author declares no competing financial interests.

### Methods

**Spin transformation.** To facilitate spin wave theory we express the spins in terms of local axes, such that the  $z$ -axis coincides with the spin direction. This can be done by performing a local rotation about the  $z$ -axis by the spin orientated angles  $\theta_i$ . Due to spin canting induced either by an external magnetic field or an in-plane DMI we perform another rotation about  $y$ -axis by the angle  $\vartheta$ . The total rotation matrix is given by

$$\mathcal{R}_z(\theta_{i,\ell}) \cdot \mathcal{R}_y(\vartheta) = \begin{pmatrix} \cos \theta_{i,\ell} \cos \vartheta & -\sin \theta_{i,\ell} & \cos \theta_{i,\ell} \sin \vartheta \\ \sin \theta_{i,\ell} \cos \vartheta & \cos \theta_{i,\ell} & \sin \theta_{i,\ell} \sin \vartheta \\ -\sin \vartheta & 0 & \cos \vartheta \end{pmatrix}, \quad (2)$$

Now, the spins transform as  $\mathbf{S}_i = \mathcal{R}_z(\theta_{i,\ell}) \cdot \mathcal{R}_y(\vartheta) \cdot \mathbf{S}'_i$ , where prime denotes the rotated frame. The classical ground state energy is given by

$$E_{\text{cl}} = 3NS^2 \left[ 2J \left( -\frac{1}{2} + \frac{3}{2} \cos^2 \vartheta \right) - \sqrt{3}D_z \sin^2 \vartheta - J_c(1 - 2 \cos^2 \vartheta) - H \cos \vartheta \right], \quad (3)$$

where  $N$  is the number of sites per unit cell, and the magnetic field is rescaled in unit of  $S$ . Minimizing this energy yields the canting angle  $\cos \vartheta = H/H_s$ , where  $H_s = 6J + 2\sqrt{3}D_z + 4J_c$  is the saturation field. The free magnon term is given by

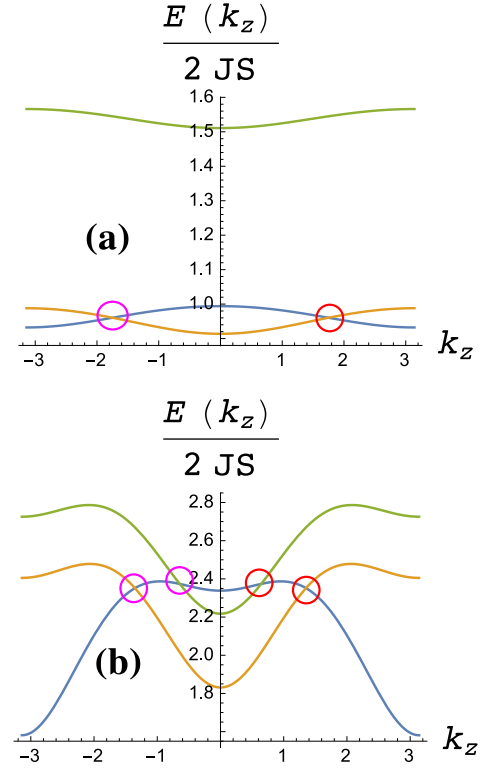


FIG. 4: **Weyl magnon bands along the  $k_z$  direction.** Here  $(k_x, k_y) = (2\pi/3, 0)$  and  $H = 0.4H_s$ . (a)  $D_z/J = 0.1$ ,  $J_c/J = 0.08$  (quasi-2D limit). (b)  $D_z/J = 0.2$ ,  $J_c/J = 1.2$  (strong 3D limit). Notice the type-II WM nodes between the topmost and lowest bands.

$$\begin{aligned} \mathcal{H}_J = J \sum_{\langle ij \rangle, \ell} & \left[ \cos \theta_{ij,\ell} \mathbf{S}'_{i,\ell} \cdot \mathbf{S}'_{j,\ell} + \sin \theta_{ij,\ell} \cos \vartheta \hat{\mathbf{z}} \cdot (\mathbf{S}'_{i,\ell} \times \mathbf{S}'_{j,\ell}) \right. \\ & \left. + 2 \sin^2 \left( \frac{\theta_{ij,\ell}}{2} \right) (\sin^2 \vartheta S'^x_{i,\ell} S'^x_{j,\ell} + \cos^2 \vartheta S'^z_{i,\ell} S'^z_{j,\ell}) \right], \end{aligned} \quad (4)$$

$$\begin{aligned} \mathcal{H}_{D_z} = -D_z \sum_{\langle ij \rangle, \ell} & \left[ \cos \theta_{ij,\ell} \cos \vartheta \hat{\mathbf{z}} \cdot (\mathbf{S}'_{i,\ell} \times \mathbf{S}'_{j,\ell}) \right. \\ & \left. - \sin \theta_{ij,\ell} (\cos^2 \vartheta S'^x_{i,\ell} S'^x_{j,\ell} + S'^y_{i,\ell} S'^y_{j,\ell} + \sin^2 \vartheta S'^z_{i,\ell} S'^z_{j,\ell}) \right], \end{aligned} \quad (5)$$

$$\begin{aligned} \mathcal{H}_{J_c} = J_c \sum_{i, \langle \ell \ell' \rangle} & \left[ \cos \theta_{\ell \ell'} \mathbf{S}'_{i,\ell} \cdot \mathbf{S}'_{i,\ell'} \right. \\ & \left. + 2 \sin^2 \left( \frac{\theta_{\ell \ell'}}{2} \right) (\sin^2 \vartheta S'^x_{i,\ell} S'^x_{i,\ell'} + \cos^2 \vartheta S'^z_{i,\ell} S'^z_{i,\ell'}) \right], \end{aligned} \quad (6)$$

$$\mathcal{H}_Z = -H \cos \vartheta \sum_{i,\ell} S'^z_{i,\ell}, \quad (7)$$

where  $\theta_{\alpha\beta} = \theta_\alpha - \theta_\beta$ . For antiferromagnetic interlayer coupling  $J_c > 0$  we have that  $\theta_{\ell \ell'} = \pi$ . For ferromagnetic interlayer  $J_c < 0$  and  $\theta_{\ell \ell'} = 0$ , therefore only the

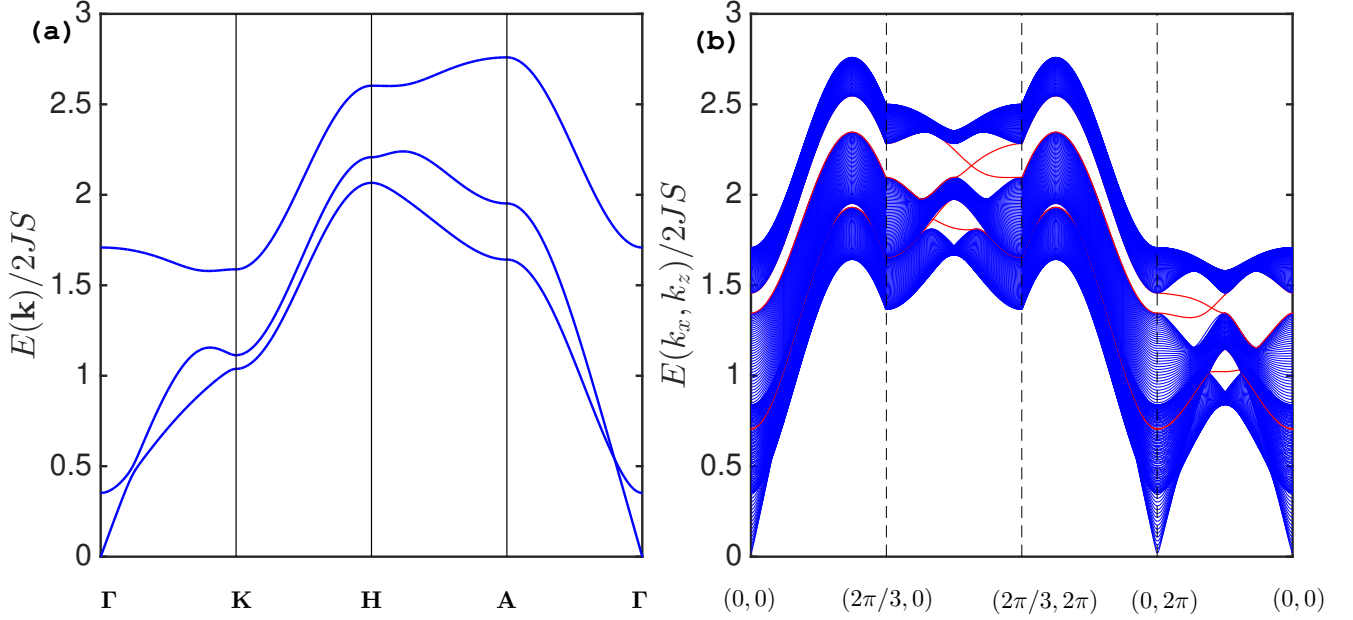


FIG. 5: **Bulk magnon bands and surface states in ferromagnetically coupled stacked kagomé antiferromagnets with nonzero scalar spin chirality.** (a) Bulk magnon bands along the BZ paths. (b) (010)-projected magnon surface states. The parameters are  $D_z/J = 0.2$ ,  $|J_c|/J = -0.5$ ,  $H = 0.3H_s$

first term in the  $J_c$  term is nonzero. The scalar spin chirality of the non-coplanar (umbrella) spin configurations defined as  $\chi_{ijk,l} = \mathbf{S}'_{i,\ell} \cdot (\mathbf{S}'_{j,\ell} \times \mathbf{S}'_{k,\ell})$  is induced only within the kagomé planes.

**Holstein-Primakoff transformation.** Next, we introduce the Holstein-Primakoff bosons:  $S_{i,\ell}^z = S - a_{i,\ell}^\dagger a_{i,\ell}$ ,  $S_{i,\ell}^+ \approx \sqrt{2S} a_{i,\ell} = (S_{i,\ell}^-)^\dagger$ , where  $S_{i,\ell}^\pm = S_{i,\ell}^x \pm iS_{i,\ell}^y$  and  $a_{i,\ell}^\dagger$  ( $a_{i,\ell}$ ) are the bosonic creation (annihilation) operators. In the following we consider the case  $J_c > 0$ . The case  $J_c < 0$  can be derived in a similar way. The magnon hopping Hamiltonians are given by

$$\begin{aligned} \mathcal{H}_{J-D_z} = S \sum_{\langle ij \rangle, \ell} [t^z (a_{i,\ell}^\dagger a_{i,\ell} + a_{j,\ell}^\dagger a_{j,\ell}) \\ + t^r (e^{-i\phi_{ij,\ell}} a_{i,\ell}^\dagger a_{j,\ell} + h.c.) + t^o (a_{i,\ell}^\dagger a_{j,\ell}^\dagger + h.c.)] \end{aligned} \quad (8)$$

$$\begin{aligned} \mathcal{H}_{J_c} = S \sum_{i,\ell} t_c^z a_{i,\ell}^\dagger a_{i,\ell} \\ + S \sum_{i, \langle \ell \ell' \rangle} [t_c^r (a_{i,\ell}^\dagger a_{i,\ell'} + h.c.) + t_c^o (a_{i,\ell}^\dagger a_{i,\ell'}^\dagger + h.c.)], \end{aligned} \quad (9)$$

$$\mathcal{H}_Z = H \cos \vartheta \sum_{i,\ell} a_{i,\ell}^\dagger a_{i,\ell} \quad (10)$$

The solid angle subtended by three non-coplanar spins is given by  $\phi_{ij} = \pm\phi$ , where  $\phi = \tan^{-1}[t_2^z/t_1^r]$ . The param-

eters of the tight binding model are given by

$$t^z = -\left[ J \left( -\frac{1}{2} + \frac{3}{2} \cos^2 \vartheta \right) - \frac{\sqrt{3}}{2} D_z \sin^2 \vartheta \right], \quad (11)$$

$$t^r = \sqrt{(t_1^r)^2 + (t_2^r)^2}, \quad (12)$$

$$t_1^r = J \left[ -\frac{1}{2} + \frac{3}{4} \sin^2 \vartheta \right] - \frac{\sqrt{3} D_z}{2} \left( 1 - \frac{\sin^2 \vartheta}{2} \right), \quad (13)$$

$$t_2^r = -\frac{\cos \vartheta}{2} (\sqrt{3} J - D_z), \quad (14)$$

$$t^o = \frac{\sin^2 \vartheta}{4} (3J + \sqrt{3} D_z), \quad (15)$$

$$t_c^z = -2J_c \cos 2\vartheta, \quad t_c^r = -J_c \cos^2 \vartheta, \quad t_c^o = J_c \sin^2 \vartheta. \quad (16)$$

Next, we Fourier transform into momentum space using the basis vector  $\psi_{\mathbf{k}}^\dagger = (a_{\mathbf{k}1}^\dagger, a_{\mathbf{k}2}^\dagger, a_{\mathbf{k}3}^\dagger, a_{-\mathbf{k}1}, a_{-\mathbf{k}2}, a_{-\mathbf{k}3})$ . The resulting Hamiltonian is given by

$$\mathcal{H}(k_{\parallel}, k_z) = 2S \begin{pmatrix} \mathcal{G}^0(k_z) + \mathcal{G}^r(k_{\parallel}) & \mathcal{G}^o(k_{\parallel}, k_z) \\ \mathcal{G}^o(k_{\parallel}, k_z) & \mathcal{G}^0(k_z) + \mathcal{G}^r(k_{\parallel}) \end{pmatrix}. \quad (17)$$

where  $\mathbf{k} = (k_{\parallel}, k_z)$  and  $k_{\parallel} = (k_x, k_y)$ . The  $\mathcal{G}$  matrices are given by  $\mathcal{G}^0(k_z) = [\sqrt{3} D_z + J + J_c + t_c^r \cos k_z] \mathbf{I}_{3 \times 3}$

$$\mathcal{G}^r(k_{\parallel}) = t^r \begin{pmatrix} 0 & \cos k_{\parallel}^1 e^{-i\phi} & \cos k_{\parallel}^3 e^{i\phi} \\ \cos k_{\parallel}^1 e^{i\phi} & 0 & \cos k_{\parallel}^2 e^{-i\phi} \\ \cos k_{\parallel}^3 e^{-i\phi} & \cos k_{\parallel}^2 e^{i\phi} & 0 \end{pmatrix}, \quad (18)$$

$$\mathcal{G}^o(k_{\parallel}, k_z) = \begin{pmatrix} t_c^o \cos k_z & t^o \cos k_{\parallel}^1 & t^o \cos k_{\parallel}^3 \\ t^o \cos k_{\parallel}^1 & t_c^o \cos k_z & t^o \cos k_{\parallel}^2 \\ t^o \cos k_{\parallel}^3 & t^o \cos k_{\parallel}^2 & t_c^o \cos k_z \end{pmatrix}, \quad (19)$$

where  $k_{\parallel}^i = k_{\parallel} \cdot \mathbf{a}_i$ , with  $\mathbf{a}_1 = \hat{x}$ ,  $\hat{\mathbf{a}}_2 = \hat{x}/2 + \sqrt{3}\hat{y}/2$ , and  $\hat{\mathbf{a}}_3 = -\hat{x}/2 + \sqrt{3}\hat{y}/2$ . The momentum space Hamiltonian of  $J_c < 0$  can be derived in a similar way.

The magnon bands are obtained by numerically diagonalizing  $\mathcal{H}(k_{\parallel}, k_z)$  using the generalized Bogoliubov transformation.

**Locations of Weyl magnon nodes.** At  $\Gamma_1 = (k_x, k_y) = (\pm 2\pi/3, 0)$  and  $\Gamma_2 = (k_x, k_y) = (0, 0)$  the eigenvalues of the Hamiltonian can be found exactly as a function  $k_z$ .

At  $\Gamma_1$  the energy bands are given by

$$\begin{aligned} [E_0(k_z)]^2 &= \frac{1}{2} \left[ 2(\mathcal{G}^0(k_z))^2 + (t^r)^2 - (t_c^o)^2 - 2(t^o)^2 \right. \\ &\quad + 4t_c^o t^o \cos(k_z) - (t_c^o)^2 \cos(2k_z) \\ &\quad \left. - 4t^r \mathcal{G}^0(k_z) \cos(\phi) + (t^r)^2 \cos(2\phi) \right] \quad (20) \end{aligned}$$

$$\begin{aligned} [E_{\pm}(k_z)]^2 &= \frac{1}{2} \left[ 2(\mathcal{G}^0(k_z))^2 + 2(t^r)^2 - 2(t_c^o)^2 - (t^o)^2 \right. \\ &\quad - 2t_c^o \{2t^o \cos(k_z) + t_c^o \cos(2k_z)\} \\ &\quad + 4t^r \mathcal{G}^0(k_z) \cos(\phi) - (t^r)^2 \cos(2\phi) \\ &\quad \left. \pm 2\sqrt{3}t^r \sin(\phi) \{2\mathcal{G}^0(k_z) + t^r \cos(\phi)\} \right], \quad (21) \end{aligned}$$

where subscript 0 denotes lowest band, whereas  $\pm$  denotes middle and topmost bands respectively.

At  $\Gamma_2$  the energy bands are given by

$$\begin{aligned} [E_0(k_z)]^2 &= \frac{1}{2} \left[ 2(\mathcal{G}^0(k_z))^2 + (2t^r)^2 - (t_c^o)^2 - 2(2t^o)^2 \right. \\ &\quad - t_c^o \{8t^o \cos(k_z) + t_c^o \cos(2k_z)\} \\ &\quad \left. + 8t^r \mathcal{G}^0(k_z) \cos(2\phi) + (2t^r)^2 \cos(2\phi) \right] \quad (22) \end{aligned}$$

$$\begin{aligned} [E_{\pm}(k_z)]^2 &= \frac{1}{2} \left[ 2(\mathcal{G}^0(k_z))^2 + (2t^r)^2 - (t_c^o)^2 - 2(t^o)^2 \right. \\ &\quad + 4t_c^o t_c^o \cos(k_z) - (t_c^o)^2 \cos(2k_z) \\ &\quad - 4t^r \mathcal{G}^0(k_z) \cos(\phi) - 2(t^r)^2 \cos(2\phi) \\ &\quad \left. \pm 4\sqrt{3}t^r \sin(\phi) \{\mathcal{G}^0(k_z) - t^r \cos(\phi)\} \right]. \quad (23) \end{aligned}$$

The WM nodes correspond to the points where the magnon bands cross linearly with each other along the  $k_z$  momentum direction. The lowest and middle magnon bands cross linearly at  $(\pm 2\pi/3, 0, k_W^1)$  and  $(0, 0, k_W^2)$ , where  $k_W^1 = \pm \cos^{-1}(\alpha_1/\beta_1)$  and  $k_W^2 = \pm \cos^{-1}(\alpha_2/\beta_2)$ ,

$$\begin{aligned} \alpha_1 &= 3(t^o)^2 + 12t^r \cos(\phi)(1 + \sqrt{3}D_z) + 12J_c t^r \cos(\phi) \\ &\quad - 3(t^r)^2 \cos(2\phi) + 4\sqrt{3}t^r \sin(\phi) + 12D_z t^r \sin(\phi) \\ &\quad + 4\sqrt{3}J_c t^r \sin(\phi) + \sqrt{3}(t^r)^2 \sin(2\phi), \quad (24) \end{aligned}$$

$$\beta_1 = 4[3t_c^o t^o - 3t^r t_c^r \cos(\phi) - \sqrt{3}t^r t_c^r \sin(\phi)], \quad (25)$$

$$\begin{aligned} \alpha_2 &= -3(t^o)^2 + t^r \left[ 6(1 + \sqrt{3}D_z + J_c) \cos(\phi) + 3t^r \cos(2\phi) \right. \\ &\quad \left. + 2\{3D_z + \sqrt{3}(1 + J_c - t^r \cos(\phi))\} \sin(\phi) \right], \quad (26) \end{aligned}$$

$$\beta_2 = 6t_c^o t^o - 2t^r t_c^r \{3 \cos(\phi) + \sqrt{3} \sin(\phi)\}. \quad (27)$$

The topmost and lowest magnon bands cross linearly at  $(\pm 2\pi/3, 0, k_W^3)$  and  $(0, 0, k_W^4)$ , where  $k_W^3 = \pm \cos^{-1}(\alpha_3/\beta_3)$ ,  $k_W^4 = \pm \cos^{-1}(\alpha_4/\beta_4)$

$$\begin{aligned} \alpha_3 &= 3(t^o)^2 + 12t^r \cos(\phi)(1 + \sqrt{3}D_z) + 12J_c t^r \cos(\phi) \\ &\quad - 3(t^r)^2 \cos(2\phi) - 4\sqrt{3}t^r \sin(\phi) - 12D_z t^r \sin(\phi) \\ &\quad - 4\sqrt{3}J_c t^r \sin(\phi) - \sqrt{3}(t^r)^2 \sin(2\phi), \quad (28) \end{aligned}$$

$$\beta_3 = 4[3t_c^o t^o - 3t^r t_c^r \cos(\phi) + \sqrt{3}t^r t_c^r \sin(\phi)], \quad (29)$$

$$\begin{aligned} \alpha_4 &= -3(t^o)^2 + t^r \left[ 6(1 + \sqrt{3}D_z + J_c) \cos(\phi) + 3t^r \cos(2\phi) \right. \\ &\quad \left. + 2\{3D_z - \sqrt{3}(1 + J_c - t^r \cos(\phi))\} \sin(\phi) \right], \quad (30) \end{aligned}$$

$$\beta_4 = 6t_c^o t^o - 2t^r t_c^r \{3 \cos(\phi) - \sqrt{3} \sin(\phi)\}. \quad (31)$$

Figures 2a and b show the WM bands along the  $k_z$  direction at  $(k_x, k_y) = (2\pi/3, 0)$ . We see that WM nodes persists in the noncoplanar quasi-2D limit for very small  $J_c/J = 0.08$  (a). In the strongly coupled limit (maybe unrealistic)  $J_c/J = 1.2$  (b) the topmost and lowest bands form type-II WM nodes. For ferromagnetically coupled antiferromagnets i.e.  $J_c < 0$  there are no discernible WM nodes as shown in Fig. 5. Rather, the system is a topological (Chern) magnon insulator with gapless surface states.